

The detection of nanoscale membrane bending with polarized localization microscopy

A. M. Kabbani and C. V. Kelly

ABSTRACT

The curvature of biological membranes at the nanometer scale is critically important for vesicle trafficking, organelle morphology, and disease propagation. The initiation of membrane bending occurs at a length scale that is irresolvable by most super-resolution optical microscopy methods. This manuscript reports the development of polarized localization microscopy (PLM), a pointillist optical imaging technique for the detection of nanoscale membrane curvature in correlation with single-molecule dynamics and molecular sorting. PLM combines polarized total internal reflection fluorescence microscopy (TIRFM) and single-molecule localization microscopy to reveal membrane orientation with sub-diffraction-limited resolution without reducing localization precision by point spread function (PSF) manipulation. Membrane curvature detection with PLM requires fewer localization events to detect curvature than 3D single-molecule localization microscopy (*e.g.*, PALM or STORM), which enables curvature detection 10x faster via PLM. With rotationally confined lipophilic fluorophores and the polarized incident fluorescence excitation, membrane-bending events are revealed with super-resolution. Engineered hemispherical membrane curvature with a radii ≥ 24 nm was detected with PLM and individual fluorophore localization precision was 13 ± 5 nm. Further, deciphering molecular mobility as a function of membrane topology was enabled. The diffusion coefficient of individual DiI molecules was $(25 \pm 5)x$ higher in planar supported lipid bilayers than within nanoscale membrane curvature. Through the theoretical foundation and experimental demonstration provided here, PLM is poised to become a powerful technique for revealing the underlying biophysical mechanisms of membrane bending at physiological length scales.

INTRODUCTION

Nanoscale membrane curvature is essential for many biological functions (1), including the regulation of lipid rafts (2), exocytosis/endocytosis (3), viral fusion/egress (4), nano-therapeutics (5), membrane remodeling (6), and the shedding of circulating microvesicles (7). Membrane curvature can be induced by the line tension between coexisting liquid lipid phases, the aggregation of curvature preferring molecules, the steric pressure between crowded proteins, and the molecular shape of either lipids or proteins (8–10). However, quantifying the relative contributions of these curvature-generating mechanisms at physiological length scales remains elusive due to limited experimental capabilities for detecting nanoscale bending. In this manuscript, we report the development of polarized localization microscopy (PLM), which combines single-molecule localization microscopy (SMLM) with polarized total internal reflection fluorescence microscopy (TIRFM). Polarized TIRFM distinguishes between membranes (11) and molecules (12) of varying orientation by measuring the overlap between the fluorophore's transition dipole moment and linearly polarized incident excitation light. Indocarbocyanine dyes (*e.g.*, DiI) maintain their transition dipole moment in the plane of the membrane such that DiI in membranes parallel to the coverslip is preferentially excited by incident s-polarized light and DiI in membranes vertical to the coverslip are preferentially excited by incident p-polarized light (Fig. 1) (13–15). Diffraction-limited polarized TIRFM has advanced the detection of membrane curvature despite lateral resolution limited to >200 nm (16), as demonstrated with presynaptic vesicle fusion (17) and endocytosis/exocytosis (11, 18).

Super-resolution SMLM such as fluorescence photo-activated localization microscopy ((f)PALM) and direct stochastic optical reconstruction microscopy ((d)STORM) have overcome the diffraction-limited resolution of traditional optical microscopy to provide images with a lateral resolution of <20 nm (19–22). SMLM depends on the computational localization of individual fluorophores that sparsely blink in sequential diffraction-limited images for the reconstruction of a super-resolution image. The resolution of the resulting reconstructed image depends on the localization imprecision, systematic inaccuracies, and localization density (23, 24). 3D SMLM has been implemented through the insertion of a cylindrical lens into the emission light path (25), single-fluorophore interference in a 4π configuration (26), biplane imaging (27), and emission phase manipulations (29). For these methods, information about the fluorophore vertical location requires either incorporating a precisely aligned multi-camera

interferometric detection path or sacrificing precision in lateral localization through the manipulation of the point spread function (PSF) to yield localization precisions along the z -direction (σ_z) typically double that of the xy -plane (σ_{xy}), approximately equal to 40 nm and 20 nm, respectively. Similarly, single-fluorophore orientations have been measured precisely by combinations of image defocusing, emission phase modulations, steerable filters, birefringent wedges, and advanced fitting routines (28–37). However, the optical and computational challenges of these methods limit their applicability to multicolor super-resolution imaging.

PLM provides fluorophore orientation with conventional detection optics, no sacrifice of localization precision by PSF manipulation, minimal adjustment of the excitation optics, and the use of commercial fluorophores. TIRF SMLM setups are able to perform PLM by the sole addition of a liquid crystal variable wave plate (*i.e.*, Thorlabs Inc, LCC1111-A), which controls the polarization of the excitation with computer control and minimal power lost. PLM depends on the use of rotationally confined fluorophores that maintain an orientation relative to the membrane normal (38) and photoswitch between fluorescent bright and transient dark states (39, 40), such as the indocarbocyanine dye DiI. Super-resolution images from PLM reveal the membrane vertical to the coverslip via p-polarized localization microscopy (pPLM) and membranes parallel to the coverslip via s-polarized localization microscopy (sPLM). This approach enables resolving dynamic nanoscale membrane curvature and curvature-induced variations in membrane organization and dynamics in aqueous, physiological conditions.

In this manuscript, PLM was used to detect engineered nanoscale membrane curvature and correlate curvature to single-molecule trajectories. PLM provided visualization of nanoscale curvature in agreement with theoretical predictions. PLM was demonstrated to provide order-of-magnitude improvements in detection and resolution of membrane curvature. Curvature in model membranes was engineered by draping supported lipid bilayers (SLBs) over nanoparticles (NPs) of known sizes, ranging in radius (r_{NP}) from 24 to 70 nm. The resulting membrane curvature and curvature-influenced diffusion of individual lipids were resolved. In sum, these studies demonstrate the capabilities of PLM to advance optical imaging capacities while providing order-of-magnitude improvements in spatial and temporal resolution than comparable SMLM techniques.

MATERIALS AND METHODS

Sample dish preparation

Glass bottom dishes (MatTek Corp.) were immersed in 7x detergent overnight, rinsed with diH₂O (18.2 MΩ-cm, EMD Millipore Corp.), bath sonicated for 30 min, dried with nitrogen gas, and cleaned by air plasma (Harrick Plasma Inc.). NPs were diluted in diH₂O, sonicated for 15 min, and deposited on a glass coverslip. NP sedimentation occurred for 10 min to achieve a density of 0.02 NPs/μm². Separate polystyrene NPs were used for both engineering membrane curvature and tracking stage drift. The index of refraction of bulk polystyrene is 1.59. NPs for creating membrane curvature were either 26 nm radius, $\lambda_{ex} = 647$ nm (FluoSpheres, Life Technologies); 51 nm radius, $\lambda_{ex} = 405$ nm (FluoSpheres, Life Technologies); or 70 nm radius, $\lambda_{ex} = 488$ nm (Fluoro-Max, Fisher Scientific). NPs for detecting stage drift (100 nm diameter, TetraSpeck, Life Technologies) were fluorescent in all color channels. Dishes were placed on a 55 °C hot plate for 5 min to ensure their stability on the coverslip. NP shape after exposure to the hotplate was confirmed by scanning electron microscopy (Fig. S1).

Supported lipid bilayer formation

Giant unilamellar vesicles (GUVs) of primarily 1-palmitoyl-2-oleoyl-sn-glycero-3-phosphocholine (POPC, Avanti Polar Lipids, Inc.) labeled with 0.3 mol% 1,1'-didodecyl-3,3,3',3'-tetramethylindocarbocyanine perchlorate (DiI, Life Technologies) were prepared by electro-formation, as described previously (41). Details on the GUV formation method are provided in the supplemental material. This fluorophore density yielded 110 nm² of bilayer per DiI molecule. The interaction between the GUVs with the plasma cleaned glass coverslip resulted in bursting of the GUVs and the formation of patches of SLB over the glass and NPs. This method of SLB creation proved to create more uniform SLBs over the NPs than SLBs formed by the fusion of large unilamellar vesicles (LUVs). The detailed methods for LUV creation are provided in the Supplemental Material.

Optical setup

PLM was performed with an inverted IX83 microscope with Zero-Drift Correction and a 100x, 1.49NA objective (Olympus Corp.) on a vibration-isolated optical table. Four continuous wave diode lasers were incorporated at wavelengths 405, 488, 561, and 647 nm, each with at least 120 mW max power for fluorescence excitation. The excitation polarization was rotated

with computer-controlled liquid crystal wave plate (Thorlabs Inc, LCC1111-A). The extinction ratio for each polarization at a certain liquid crystal input voltage is shown in the supplemental Material (Fig. S2). The ratio of the laser polarization for P/S and S/P incident upon the sample was 207:1 and 54:1, respectively, at the optimal liquid crystal wave plate voltages for each imaging condition.

The different emission wavelengths are individually selected with a filter wheel (LB10-W32-Y73, Sutter Instrument Co.) capable of 40 ms changes between filters specific for the emission ranges between the laser wavelengths. Image acquisition was performed with an iXon-897 Ultra EMCCD camera (Andor Technology) proceeded by emission filters (BrightLine single-band bandpass filters, Semrock, Inc.), a 4-band notch filter (ZET405/488/561/640m, Chroma Corp.), and a 2.5x magnification lens (Olympus Corp). This setup provided high laser power (>80 mW) at each polarization and integrated computer control of all equipment via custom LabVIEW routines (National Instruments Corp.).

Imaging procedure

Exposure of the sample to >80 mW of excitation light with $\lambda_{ex} = 561$ nm for 3 s resulted in converting most of the DiI from the fluorescent state 'on' to the transient non-fluorescent, dark state 'off' and provided steady state fluorophore blinking. The 'on' fluorophores were imaged at a density of <1 fluorophore/ μm^2 . Sequential movies were acquired with alternating p-polarized TIRF (pTIRF) excitation at $\lambda_{ex} = 561$ nm for pPLM and s-polarized TIRF (sTIRF) excitation at $\lambda_{ex} = 561$ nm for sPLM. Between 10,000 and 30,000 frames were acquired for a cropped region of interest in each polarization, at a frame rate of 50 Hz and 18 ms acquisition time per frame. Details of the imaging buffer are provided in the Supplemental Material.

Single-fluorophore localizations

The analysis of the raw, diffraction-limited images included low-pass Gaussian filtering, median background subtraction, lateral stage drift correction, and the fitting of each isolated fluorophore images via the ImageJ plug-in ThunderSTORM (42). ThunderSTORM provided the single fluorophore positions, localization uncertainty, and photon per fluorophores for further analysis. A threshold value 100 photons per fluorophores was used to keep only the bright localizations for further analysis. Single-molecule DiI localizations had 13 ± 5 nm precision

(Table S1, Fig. S3). The localizations from s- and pTIRF excitation were analyzed separately to reconstruct separate super-resolution images for each polarization.

Single-particle tracking (SPT)

The sequential localizations of single fluorophores were analyzed to reveal the diffusion rate of individual molecules versus membrane topography. The individual fluorophore trajectories projected onto the imaging plane were identified with custom MATLAB code. Single-fluorophore localizations were linked as a trajectory if they were in sequential frames, within 500 nm of each other, and there was no alternative localization for linking within 1 μm . The single-molecule step lengths (v) were grouped based on their distance from the NP center, and their normalized distribution was fit to a 2D Maxwell-Boltzmann distribution (Eq. 1) as would be expected for 2D Brownian diffusion, to find the fit diffusion coefficient (D_{fit}).

$$P(v) = \frac{v}{2D_{fit}\Delta t} e^{\frac{-v^2}{4D_{fit}\Delta t}} \quad (\text{Eq. 1})$$

The projection of the lipid trajectories onto the imaging plane yielded a decrease in their apparent step lengths depending on the membrane tilt (θ); this effect is considered in the simulations of single molecule trajectories described below. The localization imprecision ($\sigma_r = 13 \pm 5$ nm) increased the apparent step lengths. A camera blur was caused by the single-frame exposure time (t_{exp}) being a significant fraction of the time between frames (Δt) (43, 44). The diffusion coefficient (D) was calculated from D_{fit} according to

$$D = (D_{fit} - \frac{\sigma_r^2}{2\Delta t}) / (1 - \frac{t_{exp}}{3\Delta t}). \quad (\text{Eq. 2})$$

with $\sigma_r = 13$ nm, $\Delta t = 20$ ms, and $t_{exp} = 18$ ms. If $D_{fit} = 0.5 \mu\text{m}^2/\text{s}$ then $D = 0.7 \mu\text{m}^2/\text{s}$ or if $D_{fit} = 0.1 \mu\text{m}^2/\text{s}$ then $D = 0.13 \mu\text{m}^2/\text{s}$. Since the microscopy methods used here reveal only the z -projection of the diffusion, D calculated from Eq. 2 is reported as D_{xy} to emphasize that only the diffusion through the xy -plane has been measured. Diffusion coefficients from SPT are typically extracted by fitting the mean squared displacement versus Δt . However, fitting a whole trajectory to a single diffusion coefficient blurs the effects of nanoscale curvature with the lipid trajectory sampling both curved and flat membranes (44). Therefore, in the current study, a single step analysis approach was adopted to study the dynamics of lipids diffusing between curved and flat membrane.

Modeled membrane topography and diffusion

The membrane topography was simulated by smoothly connecting the spherical NP coating to a planar sheet with no less than a 20 nm radius of curvature. With custom MATLAB routines, a random distribution of points on these simulated topographies mimicked the possible 3D locations of localized fluorescent lipids. These points were used to reconstruct simulated PLM images and lipid trajectories by incorporating the localization probabilities and localizations impressions and inaccuracies detailed in the Supplemental Material.

RESULTS

Theory of PLM

PLM depends on the relative orientation between the DiI fluorescence dipole moment (μ) with the fluorescence excitation light (E). The coordinate frame was defined such that the coverslip-water interface is in the xy -plane with $z = 0$. The local membrane orientation is represented by the polar (θ) and azimuthal (ϕ) angles of the membrane normal vector relative to the microscope coordinate frame. Relative to the membrane normal, the DiI fluorescence dipole moment experiences a polar tilt (β) and azimuthal rotation (ψ) (Fig. 1D). Therefore, the Cartesian components of μ are

$$\begin{aligned}\mu_x &= \cos \theta \cos \phi \sin \beta \cos \psi - \sin \phi \sin \beta \sin \psi + \sin \theta \cos \phi \cos \beta, \\ \mu_y &= \cos \theta \sin \phi \sin \beta \cos \psi + \cos \phi \sin \beta \sin \psi + \sin \theta \sin \phi \cos \beta, \\ \mu_z &= \cos \theta \cos \beta - \sin \theta \sin \beta \cos \psi,\end{aligned}\quad (\text{Eq. 3})$$

as shown previously (14). The polar tilt of DiI in the membrane has been previously measured to be $\beta = 69^\circ$. Changing β by 5° has a <5% effect on these results (18). The azimuthal rotation of DiI samples all angles within 0.2 ns (14), resulting in an averaging over ψ for the 100s of excitation events that occur during the 18 ms single-frame exposure time. The high numerical objective used in these experiments (NA = 1.49) yields collection efficiency consistent within 10% for the emission of all fluorophore orientations (18).

Within our experimental setup, the p-polarized evanescent field (E_p) is elliptically polarized in the xz -plane and the s-polarized evanescent field (E_s) is linearly polarized in the y -plane according to

$$E_p = E_p^o (0.5x + 1.9iz) \cdot \exp\left(\frac{-z}{2d}\right),$$

$$\mathbf{E}_s = E_s^o (1.7y) \cdot \exp\left(\frac{-z}{2d}\right), \quad (\text{Eq. 4})$$

where E_p^o and E_s^o represent the magnitude of the p- and s-polarized incident electric field, respectively (14, 45). The penetration depth of the evanescent field (d) was 124 nm, as determined by the excitation incident angle ($\theta_i = 65^\circ$), excitation wavelength ($\lambda_{ex} = 561$ nm), and the indices of refraction of the sample and glass (1.33 and 1.52, respectively). Approximating \mathbf{E}_p to have no x -component induces 7% error and simplifies the intensity of excitation for each DiI molecule as a function of the membrane orientation. The corresponding intensities are then set equal to $I_p = (\mu_z \cdot \mathbf{E}_p)^2$ and $I_s = (\mu_y \cdot \mathbf{E}_s)^2$ for p- and s-polarized excitation, respectively.

Diffraction-limited polarized TIRFM compares I_p and I_s directly. PLM incorporates these intensities into the localization probability and provides increased sensitivity to changes in fluorophore orientation. Individual fluorophores demonstrated an exponential distribution of detected brightness with the average fluorophore brightness proportional to I_p or I_s (Fig. S3). Only fluorophores with a detected brightness greater than a detection threshold (B_0) were localized for inclusion in the PLM results. The probability of detecting a DiI molecule as a function of membrane orientation (θ, φ), DiI orientation with the membrane (β, ψ), and height above the coverslip (z) was approximated as

$$P_p = \exp\left(\frac{-B_0}{3.6\langle\mu_z^2\rangle\exp(-z/d)}\right),$$

$$P_s = \exp\left(\frac{-B_0}{2.9\langle\mu_y^2\rangle\exp(-z/d)}\right), \quad (\text{Eq. 5})$$

for p- and s-polarized excitation, respectively, where $\langle \rangle$ represents the average over all ψ . Since the variation in membrane height throughout this study was smaller than the width of the objective focal plane (200 nm), no change in detection probably as a function of distance from the focal plane of the objective was incorporated into this analysis. B_0 was set to match these theoretical results to the experimental results. Increasing the brightness threshold increases pPLM sensitivity to θ . pPLM yields the magnitude of θ and no information on φ . sPLM results depend on both θ and φ . Neither the sign of θ nor the value of φ may be determined with only the

z -polarized and y -polarized excitations; however, resolving changes to θ across a sample is sufficient for detecting membrane curvature.

P_s and P_p were compared to the expected detection probability for hypothetical unpolarized TIR illumination (P_{uTIR}) and unpolarized epifluorescence illumination (P_{uEPI}). The unpolarized illumination assumes all fluorophore orientations had a 50% overlap between the fluorescent dipole moment and exciting electric field direction such that there is no θ , φ , β , or ψ dependence on P_{uTIR} or P_{uEPI} . In these simulations of unpolarized illumination, we assume that the fluorophore is randomly tumbling as if it is bound by a long flexible linker. Accordingly, P_{uEPI} is a constant for all sample variables with no z dependence and

$$P_s = \exp\left(\frac{-B_0}{2.3\exp(-z/d)}\right) \quad (\text{Eq. 6})$$

The presence of membrane curvature affects the local density of localizations in the z -projection for unpolarized illumination due to the local increase in membrane area per pixel in the xy -plane.

Comparison between SMLM methods

Membrane topologies were simulated with these detection probabilities to demonstrate the effects of polarization and total internal reflection (TIR) in super-resolution imaging. The sensitivity of pPLM, sPLM, unpolarized TIR-SMLM, unpolarized Epi-SMLM, and unpolarized 3D-TIR-SMLM to membrane budding was calculated. A 50 nm radius membrane vesicle was simulated budding from a planar SLB (Fig. 2A), the expected number of localizations increases for all polarizations since the area of the membrane and the number of fluorophores increase at the site of budding. Illumination modes were compared by predicting the increase in the expected number of localizations for vesicle budding (Fig. 2B). The number of localizations from p-polarized excitation increased more than other polarizations because the new membrane had large θ . Upon the formation of a hemispherical membrane bud, when the top of the bud was 50 nm above the surrounding SLB, 11x more localizations would be detected by pPLM because of the presence of the bud. When the bud top is 100 nm away from the SLB and a complete vesicle had formed, pPLM would yield 23x more localizations while other illumination methods reveal at most 5x more localizations (Fig. 2B).

A membrane bud is identified with the statistical significance of given p-value (p) when the number of localizations at the membrane bud (N_{bud}) is greater than the average number of localizations over the planar membrane (N_{plane}) according to

$$p = e^{-N_{plane}} \sum_{i=N_{bud}}^{\infty} \frac{(N_{plane})^i}{i!}, \quad (\text{Eq. 7})$$

assuming the planar membrane provides a Poisson distribution of localizations per area. The minimum value of N_{bud} that satisfies this equation (N_{bud}^0) varies with the ratio of N_{bud} to N_{plane} , which depends on the membrane topography and excitation polarization. For instance, N_{bud} is up to 23x greater than N_{plane} for pPLM (Fig. 2B).

3D SMLM provides a minimal advantage in the ratio of N_{bud} to N_{plane} , but it does provide the height of each fluorophore with an associated uncertainty ($\sigma_z \approx 40$ nm). For 3D SMLM, statistically significant bud detection occurs when the average z -value of the localizations at the bud ($\langle z_{bud} \rangle$) has a standard error of the mean (SEM) sufficiently small such that the bud may be distinguished from the surrounding planar membrane at $z = 0$, according to

$$p = 0.5 \operatorname{erfc} \left(\langle z_{bud} \rangle \frac{\sqrt{N_{bud}^0}}{\sigma_z \cdot \sqrt{2}} \right), \quad (\text{Eq. 8})$$

where erfc is the complementary error function. The integer N_{bud}^0 that satisfies Eqs. 7 and 8 for the various bud detection methods were calculated and plotted (Fig. 2C). 3D SMLM is able to reveal membrane bending by measuring the height of each localization rather than the change in a number of localizations. However, the uncertainty of each fluorophore height requires the averaging the height of multiple fluorophores in a given region to confidently detect the membrane height. Due to this uncertainty, 3D SMLM requires more localizations for detecting membrane curvature than pPLM until the bud has fully undergone vesicle fission. Further, pPLM requires only 10% of the total number of localizations required for 3D SMLM with $p = 0.0001$ when the bud top is 50 nm above the surrounding planar membrane. This corresponds to detecting membrane budding 10x faster via pPLM than 3D SMLM. Membrane curvature detection with 3D SMLM requires data averaging that further reduces sensitivity and resolution, whereas pPLM localization density itself is correlated with membrane bending. A further discussion comparing localization rate and time required to detect local membrane bending is discussed below.

The relatively small change in the number of localizations that are detected by sPLM upon membrane budding (<3.5x) provides an internal control for other possible membrane topographies. Whereas pPLM may yield a significant increase in localizations due to the bud, sPLM shows minor fluctuations across the sample. A high local density of pPLM localizations is more confidently associated with membrane bending when coincident with a nearly uniform distribution of sPLM localizations.

Resolution and sensitivity of PLM

To demonstrate the ability of PLM to detect membrane curvature, we created membrane bending by three different methods: SLBs draped over NPs (Figs. 3, S4, and S5); LUVs above an SLB (Fig. S6); and unfused GUVs adhered to the glass coverslip (Fig. S7). The best control consistency came from SLBs composed of 99.7 mol% POPC and 0.3 mol% DiI that were draped over NPs of known size to engineer a model membrane topography. Continuity of the SLB over the NP was verified with fluorescence recovery after photobleaching (FRAP) (Fig. S8). This procedure was reproduced for 37, 29, and 175 NPs of $r_{NP} = 24, 51$, and 70 nm, respectively. pPLM provided an increased density of localizations at the site of membrane curvature and the size of the nanoscale membrane bud was measured (Figs. 4 and S9). For example, the density of localizations at the curved membrane over the 70 nm NP in pPLM was $(2.2 \pm 1) \times 10^{-6}$ localizations/nm²/frame, a 27x increase over $(8.2 \pm 3) \times 10^{-8}$ for flat SLB (Fig. 5). As an important internal control, no significant increase in the number of sPLM localizations was observed with nanoparticle-induce membrane curvature (Fig. 3J), which provides a second verification that chromatic bleed through from the NP was not present and the high index of refraction of the polystyrene NP did not adversely affect the polarization of the fluorescence excitation (Fig. S10).

Comparisons between the diffraction-limited images of the fluorescent polystyrene NP, the diffraction-limited polarized TIRFM images, and the reconstructed PLM images of the membrane reveals the increased resolution and detection sensitivity provided by PLM (Fig. 3). The diffraction-limited images demonstrated the PSF of the microscope more so than the physical size of the nanoparticle or membrane curvature. However, the radius of each membrane bud ($\langle r \rangle$) was calculated from pPLM images by averaging the distance between each localization and the center of the bud (r). This calculation yielded $\langle r \rangle$ of 32 ± 4 , 50 ± 14 , and 60 ± 13 nm for

membrane draped over NPs of 24, 51, and 70 nm radii, respectively (Fig. 4). Greater consistency in $\langle r \rangle$ calculations was provided when more localizations per area were detected, as expected (Fig. S9).

The sensitivity of PLM for detecting membrane curvature was especially apparent for the SLBs draped over NPs of 24 nm radii. The faint signal from the membrane curvature in diffraction-limited pTIRFM images could have gone undetected, whereas the increased density of localizations pPLM is readily apparent (Figs. 5 and S4). pPLM provided a 6x increase in the signal to noise ratio (SNR) over diffraction-limited p-polarized TIRFM with SNR of 11 ± 9 and 1.9 ± 0.7 , respectively, where these uncertainties represent the standard deviation between events.

LUVs of with 0.3 mol% DiI were imaged with PLM. From diffraction-limited images of polarized TIRFM excitation, flat SLBs were $(1.8 \pm 0.3)x$ brighter with sTIRFM than pTIRFM with the primary variability coming from laser alignment and SLB quality. Unfused LUVs above an SLB yielded $(1.8 \pm 0.7)x$ more signal from pTIRFM than sTIRFM with the variability coming primarily from the LUV size. The combination of these factors yielded a $(3.2 \pm 0.8)x$ increase in signal for LUV detection via diffraction-limited pTIRFM versus sTIRFM. pPLM yielded a 7.6x increase in localization rate when an LUV was present over an SLB with a (50 ± 20) versus $(6.6 \pm 0.8) \times 10^{-7}$ localizations/nm²/frame in pPLM versus sPLM. The mean and standard deviation of the LUV radii was $\langle r \rangle = 54 \pm 29$ and 57 ± 21 nm as measured by pPLM and sPLM, respectively. As a demonstration of the increased sensitivity provided by PLM, 81% of the 122 LUVs that were detected in both sPLM and pPLM were not apparent with diffraction-limited pTIRFM or sTIRFM (Fig. S11). The LUVs only detected by PLM had radii shifted to smaller values of $\langle r \rangle$ of 62 ± 20 nm while LUVs detected in PLM and TIRF possessed $\langle r \rangle$ of 72 ± 10 nm.

To reveal PLM temporal resolution, an autocorrelation analysis was performed on the PLM data. Correlation analysis was performed on both sPLM and pPLM images with increasing acquisition time interval to find PLM temporal resolution for detecting membrane bending. Results reveal the increased correlation between localizations due to the curvature detection in pPLM in comparison to the more uniform localization distributions from sPLM. Localization density rate of $(1.2 \pm 0.1) \times 10^{-6}$ localizations/nm²/frame, enabled early detection of local membrane bending over the 70 nm NPs within 1 sec in pPLM with p-value of 0.0239; for a 3 sec acquisition interval, the curvature region is detected in pPLM with a p-value of 0.0002 (Fig. 6).

Localization imprecision was limited primarily by the number of photons collected from each fluorophore in each frame. The localization software, ThunderSTORM, accounted for the camera quantum efficiency and imaging noise to estimate the number of photons and the localization precision for each detected fluorophore. 1200 ± 800 photons/fluorophore/frame were acquired yielding a localization precision of 13 ± 5 nm. Further information regarding the acquired number of photons/fluorophore and the uncertainty for the different NPs sizes are provided in the supplemental information (Fig. S3 and Table S1).

Membrane bending affects lipid mobility

The same raw data from PLM that reveals nanoscale membrane bending through image reconstruction also can be interpreted to provide single-lipid trajectories relative to the membrane bending. High-throughput SPT was performed on the raw PLM data by tracking of individual fluorophores that were localized in sequential frames. Single-molecule DiI diffusion was observed with pPLM and sPLM to reveal the apparent diffusion coefficient in the *xy*-plane (D_{xy}). DiI that was detected in more than one frame was detected in 3.8 sequential frames on average. Analyzing D_{xy} as a function of location on the sample revealed the effects of membrane topology to lipid dynamics. In particular, D_{xy} versus distance from the center of the nanoparticle (r) revealed the curvature-induced slowing of the single lipid diffusion (Fig. 7). SPT of DiI yielded $D_{xy} = 0.55 \pm 0.1 \mu\text{m}^2/\text{s}$ far from the 70 nm radius NP; however, within 50 nm of the center of the NP, $D_{xy} = 0.03 \pm 0.01 \mu\text{m}^2/\text{s}$ when detected with either p- or s-polarized excitation.

The geometrical effects of diffusing on a non-planar membrane can cause the observed diffusion rate through the *xy*-plane to be significantly different from the true, local diffusion rate. For example, a simple tilt of the membrane can decrease the apparent D_{xy} by up to 50%. With localization imprecision, long imaging frame rates, sample averaging, and increased membrane area per imaging pixel, even greater ratios of D to D_{xy} are possible. By simulating the diffusion of individual DiI on the estimated membrane topography (Fig. 5C) with a constant in-membrane diffusion rate, the simulated non-planar membrane topography was unable to reproduce the experimental results while assuming a locally Brownian diffusion.

Another hypothesis tested was that a barrier to diffusion was preventing the lipids from transitioning between the planar SLB and the membrane bud. However, the incorporation of a diffusion barrier into our simulations that prevented single-lipid trajectories from crossing

between the curved membrane bud and surrounding SLB was insufficient to reproduce the experimental data. With a 50 Hz frame rate, a local $D_{xy} = 0.55 \mu\text{m}^2/\text{s}$, and $r_{NP} = 70 \text{ nm}$, a simulated diffusion barrier yielded only half of the observed decrease in D_{xy} necessary to get from the Brownian simulation to the experimental results. Additionally, FRAP results demonstrate the continuity of the membrane between the bud and the SLB (Fig. S8) and show no apparent barrier to diffusion.

Alternatively, the hypothesis was tested that the membrane curvature induced a local change in the effective membrane viscosity. This could be caused by variations in the curvature-induced changes to the lipid packing and/or the lateral membrane tensions. This hypothesis was tested via simulations with a lipid diffusion coefficient that was slower in curved membranes than planar membranes. Simulations of lipids diffusing on a planar membrane (25 ± 5)x faster than their local diffusion on the curved membrane, well reproduced our experimental data from both sPLM and pPLM SPT (Fig. 7).

DISCUSSION

Engineered membrane curvature

The method of creating SLBs primarily used in these studies incorporated the draping burst GUVs over the glass coverslip and polystyrene NPs. Draping a bilayer over NPs of known radii provided a model of physiologically similar dimensions to clathrin- and caveolin-mediated endocytosis. SLBs created by bursting GUVs were more intact and contained fewer pores than creating a bilayer via LUV fusion. However, such holes within the SLB were still feasible with this GUV-fusion method, especially when GUVs were more violently ruptured via application of GUVs to freshly plasma cleaned glass coverslips or dilution with hypotonic solutions. The continuity of the membrane between the SLB and the curvature over the NP was confirmed FRAP and long single-lipid trajectories. Both FRAP and long trajectories demonstrated that the lipids coating the NP can exchange with the lipids directly on the coverslip (Fig. S8), similar as also shown previously (46). Examination of the continuity of the bilayer over NPs was performed by assessing the pPLM data where 94% of 290 NPs surrounded by an SLB had curved membrane draping over the NP and 60% of the NPs were well isolated from other NPs for further analysis. NPs without membrane curvature could be due to the NP being on top of the bilayer rather than under it or the formation of a hole in the SLB directly surrounding the NP.

The rare occasions in which membrane curvature did not appear at a nanoparticle gives confidence that the data we interpret as membrane curvature was not an artifact caused inherently by the presence of the nanoparticle (*i.e.*, chromatic bleed through).

An alternative membrane topography examined is that of the LUVs bound to an underlying SLB, which resembles vesicle docking in endocytosis and the later stage of exocytosis that precedes vesicle fission in cells. The variation of LUV sizes obtained by extrusion was demonstrated by PLM (Fig. S11). Other studies of vesicle sizes produced by extrusion through 100 nm pores have found the average diameter of extruded LUVs to be 65 ± 30 nm (47) indicating that the extrusion process produces a variation of LUV sizes with an upper diameter limit comparable to the extruder filter pore size. Taking advantage of PLM sensitivity and resolution, our reported values are in agreement with previous reports of LUVs size distributions imaged via SEM (47).

Membrane topography over NPs

The demonstration of PLM performed here measured nanoscale hemispherical membrane curvature of an SLB draped over NPs ranging in radii from 24 to 70 nm. Prior methods of inducing nanoscale curvature utilized nanoengineered wavy glass substrates (48), microfabricated structures (49, 50), membrane tubule pulled from GUVs (51), and SLBs on deformable substrates (52, 53). However, wavy glass substrates, thick polymer structures, and lipid tubules are not compatible with TIRF excitation. The method of draping a membrane over fluorescent NPs of known size, as done here and previously (46, 54, 55), was effective for engineering nanoscale membrane curvature, testing the capabilities of PLM, and revealing the effects of curvature on lipid mobility.

A comparison between sPLM and pPLM results provided confirmation of numerous aspects of our results. At the location of the NP-induced membrane curvature, a near uniform density of localizations in sPLM was detected whereas >5 times increase of localizations in pPLM was observed (Figs. 3 and 5A). This confirms that there was no significant chromatic bleed through from the fluorescence emission of the NP, that the refraction of the excitation light by the NP did not catastrophically alter the excitation light polarization, and that there was no significant Förster resonance energy transfer between DiI and the NP disrupting the polarization dependence of the signal. However, refraction by the NP may have influenced the direction of

the DiI emission, as discussed below, but incorporation of the high index of refraction of the polystyrene nanoparticle was not necessary for theoretical reproduction of our experimental results, as further described in the Supplemental Material.

The membrane topology over the NPs depended on the adhesion between the lipids and the polystyrene NP, the adhesion between the lipids and the glass coverslip, the size of the NP, the membrane bending rigidity, the lateral membrane tension and pressure, and the packing properties of lipids (55, 56). POPC, the dominant lipid in these experiments, has no intrinsic curvature and forcing a POPC bilayer to bend would cause an unfavorable packing of the lipids. For a positive membrane curvature, the lipid tails are crowded while the head groups are stretched over more area. For a negative membrane curvature, the lipid head groups are crowded while the lipid tails are given more volume to occupy. Both of these configurations are unfavorable for POPC and apparently result in slowing the diffusion of a fluorescent lipid through the crowded environments.

We modeled the shape of the membrane over the NPs to be primarily spherical in shape with a smooth 20 nm radii of curvature bend to connect to the planar SLB (Fig. 5C). This consistent radius of curvature for the connection of the SLB on the NP to the SLB on the coverslip resulted in a tent-like transition from the top of the small NPs to the glass substrate and a neck-like feature at the transition from the large NPs to the coverslip. The tent-like membrane structure would have a bigger size than the small NPs; the neck-like membrane structure would have a smaller size than the large NPs (Figs. 4 and 5C) (55). The tent-like model may represent the initial stages of membrane bending upon the initiation of endocytosis or conclusion of exocytosis; the neck-like model represents the later stage of endocytosis or early stage of exocytosis. The agreement between the experimentally measured and theoretically predicted radial density profiles suggest the accuracy of both the membrane model and the theoretical analysis of localization probabilities (Fig. 5 and Eq. 5).

Limitations to resolution

The distribution of localizations around the nanoparticle-induced membrane buds was influenced by multiple effects that limit the experimental determination of the membrane topography, including (1) localization imprecision of the individual fluorophores, (2) anisotropic emission from the membrane-confined DiI, (3) finite localization rates, (4) NP-induced emission

lensing, (5) the fitting of multiple ‘on’ fluorophores as if they were a single fluorophore, and (6) membrane curvature motion within the sample (*i.e.*, NP or LUV drift) (Fig. S12). Each of these contributions has been theoretically tested in attempts to match theoretical predictions to the experimental observations, as described below and in the Supplemental Material. It was found that the single-fluorophore localization imprecision, anisotropic emission effects, and bud center identification proved to be the only error sources needed to theoretically reproduce the experimental data. Matching the experimental data with theoretical estimates required no NP-induced emission lensing nor multiple ‘on’ fluorophore misassessements.

The inherent inability of DiI to tumble freely within the membrane is a necessary component for polarization sensitivity and membrane orientation detection; however, it also results in an anisotropic emission and systematic inaccuracies of DiI localization. While the DiI is not rigid in one location and can explore all ψ values in addition to a tilt of $\beta = 69^\circ$, some orientation averaging occurs for each single DiI image. Even still, the anisotropic emission results in a systematic shift up to 100 nm of the single fluorophore localizations towards the center of the NP. Numerical integration yielded the magnitude and direction of the shift in localization position due to the single fluorophore orientation and height above the focal plane following the framework of Agrawal et al. (57). The expected PSF and lateral shift were estimated as a function of membrane orientation (θ and ϕ) after considering the expected fluorophore orientations within the membrane (ψ and β). Accordingly, the expected lateral shifts as a function of membrane orientation and height were calculated. This systematic shift was incorporated into our simulated image reconstruction and SPT results, proving to be critical for matching the experimental data.

The upper limit on localization rates in all SMLM methods is based on the camera frame rate and the length scale of diffraction-limited imaging. Localization rates could be increased above those reported here by increasing density of DiI in the sample, or optimizing the DiI *on*- and *off*-rates with further buffer or incident light optimization. Further, the limited final number of localizations yields uncertainty in analyzing the precise local membrane orientation and the center of the membrane bud. Here, 200 ± 100 localizations per membrane bud were collected, each with a radius of 30 to 60 nm, which resulted in an uncertainty in identifying the bud center by 3 ± 1 nm, by standard error of the mean analysis.

SMLM is based on localizing single fluorophores that are sufficiently separated for computational fitting (>200 nm apart); however, if multiple fluorophores were in close proximity to each other (<100 nm) and falsely interpreted as a single fluorophore, then systematic errors could be incorporated. Typically, this error is predictable by assuming a uniform time-averaged fluorophore density, estimating the mean separation distance between fluorophores, and calculating the probability of multiple fluorophores being within the diffraction-limited range from each other. However, for pPLM, the assumption of a uniform time-averaged fluorophore density may not be appropriate. Since the horizontal membrane comprises the majority of the sample and DiI within the horizontal membrane absorbs less excitation light, it would follow that the sample-averaged fluorescence *off*-rate would be slower with p-polarized than with s-polarized excitation. This could yield more ‘on’ fluorophores on the curved membrane than seemingly apparent. For the curved membranes examined here, if multiple fluorophore images were averaged simultaneously, the resulting localization will be shifted toward the center of the feature. The inclusion of this error caused worse fitting of our simulations to the experimental data, suggesting that the multiple ‘on’ fluorophore misassessments were not a significant component of our image reconstruction and data analysis.

Curvature affected lipid diffusion

Analyzing D_{xy} versus distance from the NP center demonstrated how the lipid diffusion slowed at the membrane buds equivalent to as if the membrane bending caused an increase in effective viscosity (r). With greater experimental sampling densities, rates, and precision, a more sophisticated simulation and analysis routine would be warranted (44). The sequential frame linking and analysis performed here resulted in the average single-lipid step sampling a distance between 60 and 200 nm, depending on the local diffusion coefficient, which is comparable to the size of the NPs. However, the curvature-dependent single-lipid step length observed here is dramatic and was able to be modeled computationally by incorporating the experimental data conditions, such as frame rate, localization precision, anisotropic inaccuracies, and membrane topography.

The diffusion of DiI apparently slowed when the membrane was curved over the NP. The change in membrane topography from flat to the curved membrane over the NP alters DiI diffusion observed in both s- and p-polarization, resulting in a decrease in the observed diffusion

coefficient within the membrane (Fig. 7). Since the diffusion analysis from the sPLM and pPLM data yielded indistinguishable effects of membrane curvature on lipid mobility, the illumination polarization did not apparently affect the observed diffusion coefficients. When a membrane is tilted ($\theta > 0$), a 2D Brownian diffuser apparently moves slower when imaged in the xy -plane; however, this geometrical effect alone was not sufficient to reproduce diffusion rates extracted from experimental data.

To account for the 20x slowing of the single-lipid trajectories at the site of nanoscale membrane budding, two hypotheses were tested. A diffusion barrier between the membrane bud and the surrounding planar SLB was not sufficient in matching the modeled and experimental data. However, combining both the geometrical effects of the tilted membrane and a curvature-dependent effective membrane viscosity yielded a strong agreement between the modeled and experimental SPT results. This analysis supports the hypothesis that DiI diffuses slower on more curved membranes due to change in membrane properties such as effective membrane viscosity or lipid packing, as suggested previously (46).

Neither the experimental data nor the simulated theoretical reproduced data for D_{xy} distinguishes between the two leaflets of the lipid bilayer. The SLBs were symmetrically labeled through the addition of DiI to the lipid mixture before GUV electroformation, and both bilayer leaflets contributed to the observed DiI diffusion rates. DiI in the outer leaflet would have minimal direct substrate interaction, whereas DiI in the inner leaflet would be in close proximity to the supporting polystyrene NP or glass coverslip. However, our control experiments have failed to find a substrate-induced slowing of the single-lipid diffusion. We have created stacked SLB structure with between 1 and 5 bilayers layered over the coverslip and we have not detected any difference in the distribution of single-lipid step lengths versus number of bilayers present; the cushioning of an SLB by additional SLBs did not apparently affect the single-lipid diffusion. Accordingly, this suggests that the substrate differences between the glass coverslip and the polystyrene nanoparticle are unlikely to affect the single-lipid step lengths reported here. Further, single-lipid diffusion has been observed to be slower when nanoscale membrane buds are formed by cholera toxin subunit B (CTxB) rather than a nanoparticle (58).

Diffusion rates measured by SPT, FRAP, and fluorescence correlation spectroscopy (FCS) show systematic variations in the measured diffusion coefficients depending on the analysis method. Comparison between these techniques requires accounting for their difference

in sensitivity to detecting mobile versus immobile diffusers, length and time scale dependent processes, and subpopulations of diffusers (43, 44). The SPT results presented here are consistent with prior SPT results and, as expected, report a slower diffusion rate than FRAP or FCS measurements (54, 59).

Future improvements to PLM

PLM is able to provide super-resolution detail on membrane orientation with improved sensitivity and resolution from comparable methods. Since PLM requires no manipulation of the fluorescence emission path or the PSF, the incorporation of PLM with SMLM in additional complementary color channels is straightforward. For example, the simultaneous super-resolution membrane orientation detection via PLM with the curvature-sorting and curvature-induction effects of CTxB is the focus of a companion manuscript in this journal (58).

It is feasible that the local membrane orientation could be evaluated by the direct mapping of acquired localizations per pixel to the PLM theory. In order to perform such analysis, a minimal localization density of 0.05 localizations/nm² would be required. PLM has the advantage of observing lipids that diffuse into the region of view from the surrounding membrane to effectively achieve unlimited labeling densities, similar to as has been previously utilized in point accumulation for imaging in nanoscale topography (PAINT) (60). Greater sampling statistics would enable finer details of membrane topology to be extracted with more statistically significant comparisons between pPLM and sPLM localization densities.

With a faster frame rate and/or decreased localization imprecision, more sophisticated SPT analyses could be performed (44). It could be instructive to analyze the single-molecule trajectories such as to extract the component of the molecular diffusion radial from the center of the bud as opposed to the diffusion component around the bud. If some membrane components accumulate at the bud neck, it is feasible that the single-molecules could diffuse quickly around the bud while slowly changing its radial distance from the bud center. Unfortunately, this analysis is not feasible at the current imaging frame rates, but it will be the focus of future work through using PLM to reveal the nanoscale effects of membrane curvature.

CONCLUSIONS

Polarized localization microscopy (PLM) is capable of detecting and resolving nanoscale membrane curvature with super-resolution and correlating this curvature to the single-molecule diffusion and molecular sorting. PLM requires no alteration of the emission path from traditional single-molecule fluorescence microscopes and incorporates no inherent sacrifice in the signal or localization precision for observing the membrane orientation. Distinct identification between membrane topology of LUVs, GUVs, and curved SLBs over NPs was observed. The nanoparticle-patterned substrate provided a means to engineering nanoscale membrane curvature of physiologically relevant dimensions. Local membrane bending regions with radii of curvature ≥ 24 nm were detected. PLM detected membrane curvature and resolved membrane topography with 1 sec of acquisition time at $(1.2 \pm 0.1) \times 10^6$ localizations/nm²/frame.

Radial line scans of pPLM localizations reveal radii of curvature of 32 ± 4 , 50 ± 14 , 60 ± 13 nm for membranes over the nanoparticles radii of 24, 51, and 70 nm, respectively. Further, a 6x increase in the SNR is obtained by PLM over traditional TIRFM. The theoretically estimated localization probabilities versus membrane orientation well reproduced experimental data. The unique spatiotemporal resolution of PLM is suited to monitor membrane structure variation with lipid and protein dynamics. We envision that this microscopy technique will provide new information for previously untestable nanoscale processes coupled with a change in membrane topography. This was demonstrated by the observation of time-dependent membrane budding initiation and growth induced by cholera toxin subunit B in quasi-one component lipid bilayers, revealing a possible mechanism of cholera immobilization and cellular internalization described further in the accompanying manuscript (58). Fundamental questions regarding nanoscale cellular processes such as clathrin-independent endocytosis, viral infections, endocytosis/exocytosis, and immunological responses are soon to be addressed with PLM. The feasibility of performing PLM on model membranes or live cells on time scales suitable for observing cellular processes permits this technique to be adopted and broadly used to probe cellular dynamics.

ACKNOWLEDGEMENTS

The authors thank Xinxin Woodward, Arun Anantharam, Dipanwita De, Henry Edelman, Rebecca Meerschaert, and Eric Stimpson for valuable discussions. A.M.K. was funded by Thomas C. Rumble Fellowship Award. Financial support was provided by Wayne State

University laboratory start-up funds, Richard J. Barber, and a CAREER award from the National Science Foundation (DMR1652316).

AUTHOR CONTRIBUTIONS

A.M.K. and C.V.K. designed the experiments, analyzed the data, and prepared the manuscript. A.M.K. performed the experiments. C.V.K. performed the simulations.

COMPETING FINANCIAL INTERESTS STATEMENT

The authors have no competing financial interests.

REFERENCES

1. McMahon, H.T., and E. Boucrot. 2015. Membrane curvature at a glance. *J. Cell Sci.* 128: 1065–1070.
2. Lingwood, D., and K. Simons. 2010. Lipid Rafts As a Membrane-Organizing Principle. *Science*. 327: 46–50.
3. Kozlov, M.M., H.T. McMahon, and L.V. Chernomordik. 2010. Protein-driven membrane stresses in fusion and fission. *Trends Biochem. Sci.* 35: 699–706.
4. Ono, A. 2010. Viruses and Lipids. *Viruses*. 2: 1236–1238.
5. Kelly, C.V., M.G. Liroff, L.D. Triplett, P.R. Leroueil, D.G. Mullen, J.M. Wallace, S. Meshinchi, J.R. Baker, B.G. Orr, and M.M. Banaszak Holl. 2009. Stoichiometry and Structure of Poly(amidoamine) Dendrimer–Lipid Complexes. *ACS Nano*. 3: 1886–1896.
6. McMahon, H.T., and J.L. Gallop. 2005. Membrane curvature and mechanisms of dynamic cell membrane remodelling. *Nature*. 438: 590–596.
7. Raposo, G., and W. Stoorvogel. 2013. Extracellular vesicles: exosomes, microvesicles, and friends. *J. Cell Biol.* 200: 373–383.
8. Baumgart, T., B.R. Capraro, C. Zhu, and S.L. Das. 2011. Thermodynamics and Mechanics of Membrane Curvature Generation and Sensing by Proteins and Lipids. *Annu. Rev. Phys. Chem.* 62: 483–506.
9. Zimmerberg, J., and M.M. Kozlov. 2006. How proteins produce cellular membrane curvature. *Nat. Rev. Mol. Cell Biol.* 7: 9–19.
10. Stachowiak, J.C., E.M. Schmid, C.J. Ryan, H.S. Ann, D.Y. Sasaki, M.B. Sherman, P.L. Geissler, D.A. Fletcher, and C.C. Hayden. 2012. Membrane bending by protein-protein crowding. *Nat. Cell Biol.* 14: 944–949.
11. Anantharam, A., D. Axelrod, and R.W. Holz. 2010. Polarized TIRFM Reveals Changes in Plasma Membrane Topology Before and During Granule Fusion. *Cell Mol. Neurobiol.* 30: 1343–1349.
12. Forkey, J.N., M.E. Quinlan, and Y.E. Goldman. 2005. Measurement of single macromolecule orientation by total internal reflection fluorescence polarization microscopy. *Biophys. J.* 89: 1261–1271.
13. Axelrod, D., T.P. Burghardt, and N.L. Thompson. 1984. Total Internal Reflection Fluorescence. *Annu. Rev. of Biophys. Bioeng.* 13: 247–268.
14. Sund, S.E., J.A. Swanson, and D. Axelrod. 1999. Cell Membrane Orientation Visualized by Polarized Total Internal Reflection Fluorescence. *Biophys. J.* 7: 2266–2283.
15. Anantharam, A., D. Axelrod, and R.W. Holz. 2012. Real-time imaging of plasma membrane deformations reveals pre-fusion membrane curvature changes and a role for dynamin in the regulation of fusion pore expansion. *J. Neurochem.* 122: 661–671.

16. Axelrod, D. 1981. Cell-substrate contacts illuminated by total internal reflection fluorescence. *J. Cell Biol.* 89: 141–145.
17. Kiessling, V., M.K. Domanska, and L.K. Tamm. 2010. Single SNARE-Mediated Vesicle Fusion Observed In Vitro by Polarized TIRFM. *Biophys. J.* 99: 4047–4055.
18. Anantharam, A., B. Onoa, R.H. Edwards, R.W. Holz, and D. Axelrod. 2010. Localized topological changes of the plasma membrane upon exocytosis visualized by polarized TIRFM. *J. Cell Biol.* 188: 415–428.
19. Betzig, E., G.H. Patterson, R. Sougrat, O.W. Lindwasser, S. Olenych, J.S. Bonifacino, M.W. Davidson, J. Lippincott-Schwartz, and H.F. Hess. 2006. Imaging Intracellular Fluorescent Proteins at Nanometer Resolution. *Science.* 313: 1642–1645.
20. Hess, S.T., T.P.K. Girirajan, and M.D. Mason. 2006. Ultra-High Resolution Imaging by Fluorescence Photoactivation Localization Microscopy. *Biophys. J.* 91: 4258–4272.
21. Rust, M.J., M. Bates, and X. Zhuang. 2006. Sub-diffraction-limit imaging by stochastic optical reconstruction microscopy (STORM). *Nat. Methods.* 3: 793–796.
22. van de Linde, S., A. Loschberger, T. Klein, M. Heidbreder, S. Wolter, M. Heilemann, and M. Sauer. 2011. Direct stochastic optical reconstruction microscopy with standard fluorescent probes. *Nat. Protoc.* 6: 991–1009.
23. Thompson, R.E., D.R. Larson, and W.W. Webb. 2002. Precise Nanometer Localization Analysis for Individual Fluorescent Probes. *Biophys. J.* 82: 2775–2783.
24. Dempsey, G.T., J.C. Vaughan, K.H. Chen, M. Bates, and X. Zhuang. June 11. Evaluation of fluorophores for optimal performance in localization-based super-resolution imaging. *Nat. Methods.* 8: 1027–1036.
25. Huang, B., W. Wang, M. Bates, and X. Zhuang. 2008. Three-Dimensional Super-Resolution Imaging by Stochastic Optical Reconstruction Microscopy. *Science.* 319: 810–813.
26. Shtengel, G., J.A. Galbraith, C.G. Galbraith, J. Lippincott-Schwartz, J.M. Gillette, S. Manley, R. Sougrat, C.M. Waterman, P. Kanchanawong, M.W. Davidson, R.D. Fetter, and H.F. Hess. 2009. Interferometric fluorescent super-resolution microscopy resolves 3D cellular ultrastructure. *Proc. Natl. Acad. Sci. U.S.A.* 106: 3125–3130.
27. Juette, M.F., T.J. Gould, M.D. Lessard, M.J. Mlodzianoski, B.S. Nagpure, B.T. Bennett, S.T. Hess, and J. Bewersdorf. 2008. Three-dimensional sub-100 nm resolution fluorescence microscopy of thick samples. *Nat. Methods.* 5: 527–529.
28. Aguet, F., S. Geissbühler, I. Märki, T. Lasser, and M. Unser. 2009. Super-resolution orientation estimation and localization of fluorescent dipoles using 3-D steerable filters. *Opt Express.* 17: 6829–6848.

29. Backlund, M.P., M.D. Lew, A.S. Backer, S.J. Sahl, G. Grover, A. Agrawal, R. Piestun, and W.E. Moerner. 2012. Simultaneous, accurate measurement of the 3D position and orientation of single molecules. *Proc Natl Acad Sci U S A.* 109: 19087–19092.
30. Backer, A.S., M.P. Backlund, M.D. Lew, and W.E. Moerner. 2013. Single-molecule orientation measurements with a quadrated pupil. *Opt Lett.* 38: 1521–1523.
31. Gould, T.J., M.S. Gunewardene, M.V. Gudheti, V.V. Verkhusha, S.-R. Yin, J.A. Gosse, and S.T. Hess. 2008. Nanoscale imaging of molecular positions and anisotropies. *Nat. Methods.* 5: 1027–1030.
32. Patra, D., I. Gregor, and J. Enderlein. 2004. Image Analysis of Defocused Single-Molecule Images for Three-Dimensional Molecule Orientation Studies. *J. Phys. Chem. A.* 108: 6836–6841.
33. Lieb, M.A., J.M. Zavislan, and L. Novotny. 2004. Single-molecule orientations determined by direct emission pattern imaging. *J. Opt. Soc. Am. B.* 21: 1210.
34. Syed, S., G.E. Snyder, C. Franzini-Armstrong, P.R. Selvin, and Y.E. Goldman. 2006. Adaptability of myosin V studied by simultaneous detection of position and orientation. *EMBO J.* 25: 1795–1803.
35. Pavani, S.R.P., M.A. Thompson, J.S. Biteen, S.J. Lord, N. Liu, R.J. Twieg, R. Piestun, and W.E. Moerner. 2009. Three-dimensional, single-molecule fluorescence imaging beyond the diffraction limit by using a double-helix point spread function. *Proc. Natl. Acad. Sci. U.S.A.* 106: 2995–2999.
36. Sick, B., B. Hecht, and L. Novotny. 2000. Orientational imaging of single molecules by annular illumination. *Phys. Rev. Lett.* 85: 4482–4485.
37. Sinkó, J., T. Gajdos, E. Czvik, G. Szabó, and M. Erdélyi. 2017. Polarization sensitive localization based super-resolution microscopy with a birefringent wedge. *Methods Appl. Fluoresc.* 5: 017001.
38. Axelrod, D. 1979. Carbocyanine dye orientation in red cell membrane studied by microscopic fluorescence polarization. *Biophys. J.* 26: 557–573.
39. Shim, S.-H., C. Xia, G. Zhong, H.P. Babcock, J.C. Vaughan, B. Huang, X. Wang, C. Xu, G.-Q. Bi, and X. Zhuang. 2012. Super-resolution fluorescence imaging of organelles in live cells with photoswitchable membrane probes. *Proc. Natl. Acad. Sci. U.S.A.* 109: 13978–13983.
40. Dempsey, G.T., M. Bates, W.E. Kowtoniuk, D.R. Liu, R.Y. Tsien, and X. Zhuang. 2009. Photoswitching Mechanism of Cyanine Dyes. *J. Am. Chem. Soc.* 131: 18192–18193.
41. Veatch, S. 2007. Electro-Formation and Fluorescence Microscopy of Giant Vesicles With Coexisting Liquid Phases. In: McIntosh T, editor. *Lipid Rafts*. Humana Press. pp. 59–72.
42. Ovesný, M., P. Křížek, J. Borkovec, Z. Švindrych, and G.M. Hagen. 2014. ThunderSTORM: a comprehensive ImageJ plug-in for PALM and STORM data analysis and super-resolution imaging. *Bioinformatics.* 30: 2389–2390.
43. Lagerholm, B.C., D.M. Andrade, M.P. Clausen, and C. Eggeling. 2017. Convergence of lateral dynamic measurements in the plasma membrane of live cells from single particle tracking and STED-FCS. *J Phys D Appl Phys.* 50: 063001.

44. Kabbani, A.M., X. Woodward, and C.V. Kelly. 2017. Revealing the effects of nanoscale membrane curvature on lipid mobility. *arXiv:1706.00087* [physics].
45. Hellen E., H. M. Fulbright R., and D. Axelrod. 1988. Total internal reflection fluorescence: theory and applications at biosurfaces. *Spectroscopic Membrane Probes*. 2: 47–79.
46. Black, J.C., P.P. Cheney, T. Campbell, and M.K. Knowles. 2014. Membrane curvature based lipid sorting using a nanoparticle patterned substrate. *Soft Matter*. 10: 2016–2023.
47. Kunding, A.H., M.W. Mortensen, S.M. Christensen, and D. Stamou. 2008. A fluorescence-based technique to construct size distributions from single-object measurements: application to the extrusion of lipid vesicles. *Biophys. J.* 95: 1176–1188.
48. Hsieh, W.-T., C.-J. Hsu, B.R. Capraro, T. Wu, C.-M. Chen, S. Yang, and T. Baumgart. 2012. Curvature Sorting of Peripheral Proteins on Solid-Supported Wavy Membranes. *Langmuir*. 28: 12838–12843.
49. Ryu, Y.-S., I.-H. Lee, J.-H. Suh, S.C. Park, S. Oh, L.R. Jordan, N.J. Wittenberg, S.-H. Oh, N.L. Jeon, B. Lee, A.N. Parikh, and S.-D. Lee. 2014. Reconstituting ring-rafts in bud-mimicking topography of model membranes. *Nat Commun*. 5.
50. Ogunyankin, M.O., D.L. Huber, D.Y. Sasaki, and M.L. Longo. 2013. Nanoscale Patterning of Membrane-Bound Proteins Formed through Curvature-Induced Partitioning of Phase-Specific Receptor Lipids. *Langmuir*. 29: 6109–6115.
51. Tian, A., and T. Baumgart. 2009. Sorting of Lipids and Proteins in Membrane Curvature Gradients. *Biophys. J.* 96: 2676–2688.
52. Sanii, B., A.M. Smith, R. Butti, A.M. Brozell, and A.N. Parikh. 2008. Bending membranes on demand: fluid phospholipid bilayers on topographically deformable substrates. *Nano Lett.* 8: 866–871.
53. Gilmore, S.F., H. Nanduri, and A.N. Parikh. 2011. Programmed Bending Reveals Dynamic Mechanochemical Coupling in Supported Lipid Bilayers. *PLoS One*. 6.
54. Cheney, P.P., A.W. Weisgerber, A.M. Feuerbach, and M.K. Knowles. 2017. Single Lipid Molecule Dynamics on Supported Lipid Bilayers with Membrane Curvature. *Membranes (Basel)*. 7: 15.
55. Roiter, Y., M. Ornatska, A.R. Rammohan, J. Balakrishnan, D.R. Heine, and S. Minko. 2008. Interaction of Nanoparticles with Lipid Membrane. *Nano Letters*. 8: 941–944.
56. Larsen, J.B., M.B. Jensen, V.K. Bhatia, S.L. Pedersen, T. Bjørnholm, L. Iversen, M. Uline, I. Szleifer, K.J. Jensen, N.S. Hatzakis, and D. Stamou. 2015. Membrane curvature enables N-Ras lipid anchor sorting to liquid-ordered membrane phases. *Nat. Chem. Biol.* 11: 192–194.
57. Agrawal, A., S. Quirin, G. Grover, and R. Piestun. 2012. Limits of 3D dipole localization and orientation estimation for single-molecule imaging: towards Green's tensor engineering. *Opt Express*. 20: 26667–26680.

58. Kabbani, A.M., and C.V. Kelly. 2017. Nanoscale membrane budding induced by CTxB on quasi-one component lipid bilayers detected by polarized localization microscopy. arXiv:1703.08865 [physics]. Biophys J Manuscript Number: 2017BIOPHYSJ307665.
59. Bag, N., D.H.X. Yap, and T. Wohland. 2014. Temperature dependence of diffusion in model and live cell membranes characterized by imaging fluorescence correlation spectroscopy. *Biochim. Biophys. Acta.* 1838: 802–813.
60. Sharonov, A., and R.M. Hochstrasser. 2006. Wide-field subdiffraction imaging by accumulated binding of diffusing probes. *Proc. Nat. Acad. Sci.* 103: 18911–18916.

FIGURE CAPTIONS

FIGURE 1 Polarized Localization Microscopy (PLM) combines the techniques of polarized TIRFM and SMLM. By controlling the linear polarization of incident excitation light, the electric field (*green arrows*) of the evanescent wave for fluorescence excitation can be either (A) vertical with p-polarized light or (B) horizontal with s-polarized light. This results in differential excitation of rotationally confined fluorophores dependent on the local membrane orientation. (C) Imaging and localizing individual blinking fluorophores in separate frames enables the reconstruction of super-resolution images with embedded information on membrane orientations. (D) The probability of localizing a DiI depends on the direction of the normal vector to the membrane (\mathbf{n}) relative to the coverslip, as described by θ and φ , as well as and the angle of the DiI dipole moment ($\boldsymbol{\mu}$) within the membrane, as described by β and ψ .

FIGURE 2 Theoretical estimates of the localization probabilities reveal the sensitivity of PLM compared to other optical methods. (A) Membranes containing buds of 50 nm radii of curvature were analyzed at varying protrusion distances from the surrounding connected planar membrane. The fractional increase in localizations due to the bud is plotted. (B) The increased number of localizations expected due to non-planar membrane shape relative to the number of localizations expected from a planar membrane demonstrated a 23x increase in localization density with pPLM, which is over 4x larger than expected for sPLM, unpolarized epifluorescence SMLM, and unpolarized total internal reflection (TIR) illumination SMLM. The fraction increase in localizations due to the bud in 3D TIR SMLM is similar to the TIR SMLM results. (C) The required number of localizations to identify a membrane bud from the surrounding SLB (N_{bud}^0) with $p = 0.0001$ are plotted for pPLM, sPLM, unpolarized TIR, and unpolarized epifluorescence SMLM from Eq. 7 and for 3D SMLM from Eq. 8.

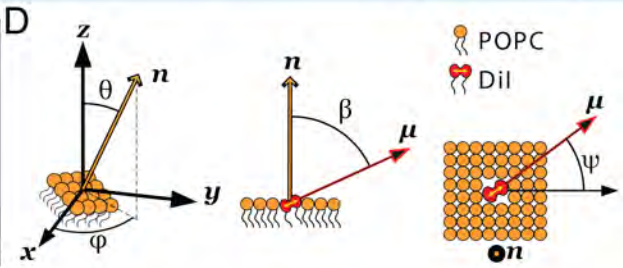
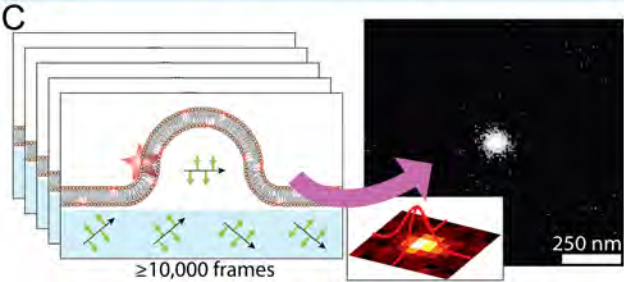
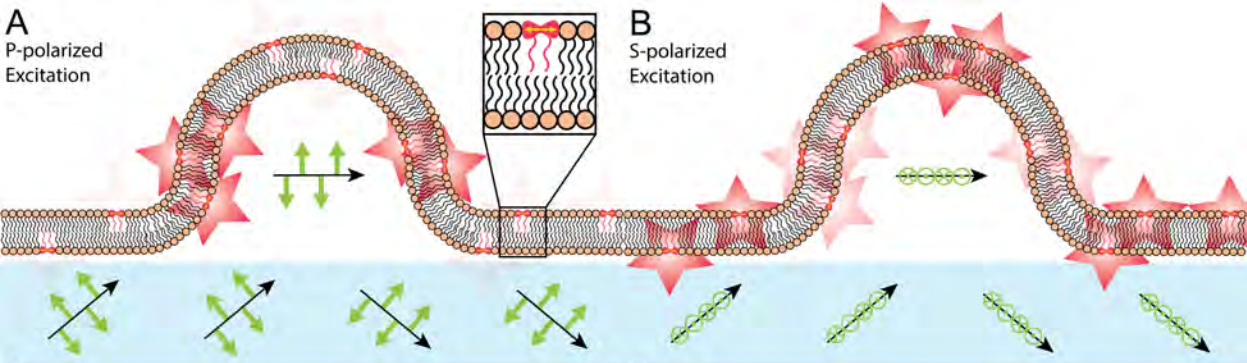
FIGURE 3 Membrane curvature was engineered by draping a supported lipid bilayer over NPs. (A) The 70 nm radius fluorescent NPs on glass were imaged with $\lambda_{ex} = 488$ nm. (B-E) The membrane was imaged with $\lambda_{ex} = 561$ nm and the differences between the polarizations provide internal controls. (B, C) Diffraction-limited p-polarized and s-polarized TIRFM image, respectively. (D, E) Reconstructed images of the membrane over the NPs presented as 2D histograms of the localizations in pPLM and sPLM, respectively. (F-J) Magnified views of the dashed regions from (A-E) show membrane curvature coincident with the nanoparticles. (I) The detected membrane curvature over the 70 nm NPs is indicated by white arrows. (I, J) A multicolored fiduciary mark is indicated by red arrows. Scale bars represent (A-E) 5 μ m and (F-J) 400 nm. The Supplemental Material provides similar results for other size and color NPs (Figs. S4 and S5), LUVs (Fig. S6), GUVs, (Fig. S7), and other magnifications of these data (Fig. S13).

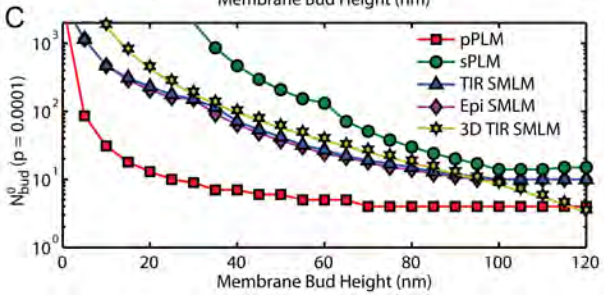
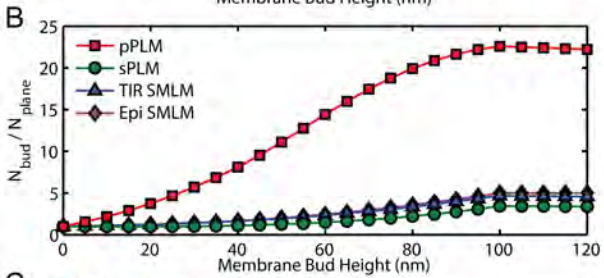
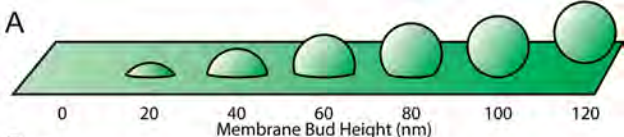
FIGURE 4: (A-C) Radial probability distribution of localizations versus distance from the center of the curved membrane (r) over NPs of $r_{NP} = 24$, 51, and 70 nm, respectively. Grey lines represent individual events and the colored lines represent the averages. Error bars represent the standard error of the mean at a given r . (D-F) Histograms of the radius for each membrane curvature event ($\langle r \rangle$) for $r_{NP} = 24$, 51, and 70 nm. Black lines represent the Gaussian fits to guide the eye. The mean of the events radii was 32 ± 4 , 50 ± 14 , 60 ± 13 nm for $r_{NP} = 24$, 51, and 70 nm, respectively.

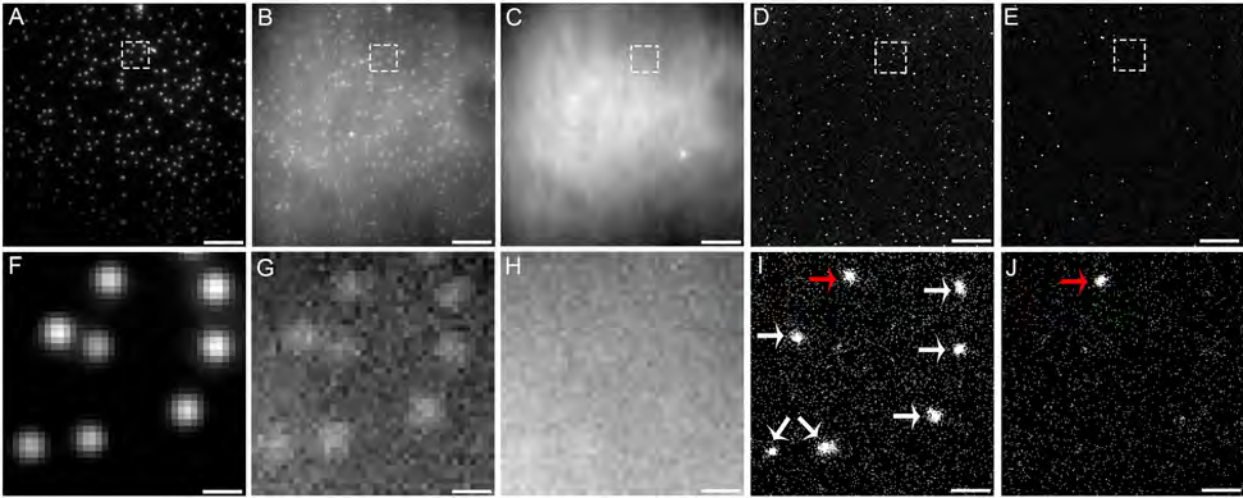
FIGURE 5 The density of localizations vs. distance from the center of the curved membrane (r) observed via (A) pPLM and (B) sPLM. Data points show the experimental results while the theoretical results are plotted as solid lines. The theoretical results assumed the membrane topography shown in (C) with a single B_0 value and out-of-focus magnitude for anisotropic inaccuracy were fit to all six data sets from Eq. 5.

FIGURE 6 Autocorrelation analysis for sPLM (black) and pPLM (red) for different acquisition time intervals. (A) Data were normalized to the first $G(r)$ value to show the detection of curvature in pPLM with smaller error bars as time interval increases in comparison to sPLM. (B) Auto-correlation $G(r)$ value at $r = 0$. The sPLM analysis provides an internal control to show the uniform bilayer analysis. An acquisition time of 1 sec is sufficient to indicate the presence of curvature in pPLM.

FIGURE 7 Single-particle tracking of DiI molecules reveals slowed diffusion at the site of nanoscale membrane curvature equally while imaged with p- or s-polarized excitation. SLBs were draped over 70 nm radius NPs. Particle locations were projected on the xy -plane and the apparent fluorophore diffusion was affected by both the 3D membrane topology and the influences of membrane curvature on DiI mobility. The fit of the distribution of step lengths to Eq. 1 yielded the apparent diffusion coefficient and the 95% confidence range, as indicated by the error bars. Neither a locally Brownian diffusion nor a simulated barrier to free diffusion surrounding the bud reproduced the experimental results. However, upon simulating a decreased local D for curved SLB slower than that of the planar SLB, the resulting simulated D_{xy} well matched the experimentally observed D_{xy} . Simulations matched experimental data when the planar SLB had a D that was $(25 \pm 5)x$ faster than the curved SLB.







Radial Probability Distribution of Localizations

